Astronomy & Astrophysics manuscript no. 3129 July 27, 2005
(DOI: will be inserted by hand later)

Detailed comparison of downflows seen both in EIT 30.4 nm and Big Bear Hα movies

A. De Groof[1], C. Bastiaensen[1], D.A.N. Müller[2,3,4], D. Berghmans[5] and S. Poedts[1]

[1] Centre for Plasma Astrophysics, K.U. Leuven, Celestijnenlaan 200B, 3001 Leuven, Belgium;
e-mail: Anik.DeGroof@wis.kuleuven.be, Stefaan.Poedts@wis.kuleuven.be
[2] Institute of Theoretical Astrophysics, University of Oslo, P.O. Box 1029 Blindern, 0315 Oslo, Norway;
e-mail: Daniel.Mueller@astro.uio.no
[3] Center of Mathematics for Applications, University of Oslo, P.O. Box 1053 Blindern, 0316 Oslo, Norway;
[4] European Space Agency, Research and Scientific Support Department c/o NASA Goddard Space Flight Center, Mail Code 612.5, Greenbelt, MD 20771, USA;
[5] Royal Observatory of Belgium, Ringlaan 3 Av. Circulaire, 1180 Brussels, Belgium;
e-mail: david.berghmans@oma.be

Received ; accepted

Abstract. An EIT shutterless campaign was conducted on 11 July 2001 and provided 120 high-cadence (68s) 30.4 nm images of the north-eastern quarter of the Sun. Systematic intensity variations are seen which appear to propagate along an off-disk loop-like structure. In this paper we study the nature of these intensity variations by confronting the EIT observations studied in De Groof et al. (2004) with simultaneous Hα images from Big Bear Solar Observatory.
With the goal to carefully co-register the two image sets, we introduce a technique designed to compare data of two different instruments. The image series are first co-aligned and later overplotted in order to visualize and compare the behaviour of the propagating disturbances in both data sets. Since the same intensity variations are seen in the EIT 30.4 nm and in the Hα images, we confirm the interpretation of De Groof et al. (2004) that we are observing downflows of relatively cool plasma. The origin of the downflows is explained by numerical simulations of "catastrophic cooling" in a coronal loop which is heated predominantly at its footpoints.

Key words. Sun: atmosphere – Sun: activity

1. Introduction

Propagating intensity variations in magnetic loop structures are often seen in the solar atmosphere and are of great importance for coronal seismology and for the understanding of coronal heating mechanisms. Some show a periodic behaviour and are most often classified as slow magneto-acoustic waves propagating along coronal loops (e.g. Aschwanden et al. 1999; Roberts 2000; De Moortel et al. 2002a,b). Others are observed in flare loops or prominences and are attributed to plasma material falling down along the magnetic legs of, respectively, a coronal loop after the eruption of a solar flare, or a prominence. Even though the characteristics of these phenomena are very different, both waves and downflows show up as propagating intensity variations. Slow magneto-acoustic waves are especially observed in high-resolution EUV images of SoHO/EIT and TRACE (17.1 nm and 19.5 nm), mostly due to density inhomogeneities along the loop when the wave passes by.
Downflows in flare loops or prominences on the other hand are usually seen in cool chromospheric lines like the Ca II line and Hα (e.g. Engvold et al. 1979; Loughhead & Bray 1984; Delone et al. 1989; Heinzel et al. 1992; Wiik et al. 1996). Since the loops/prominences are usually only partly filled with Hα or Ca II emitting material, the fine structure revealed by high spatial resolution observations consists of (a 'train' of) bright blobs moving downwards. In some exceptional cases a continuous motion from one footpoint to the other is observed.

Propagating disturbances in the EIT 30.4 nm channel (Delaboudinière et al. 1995) were first reported by De Groof et al. (2004). The EIT 30.4 nm band is dominated by the transition-region line of He II, corresponding to plasma at a temperature of about 60000K. However the spectral width of the EIT 30.4 nm filter leads to contributions of other lines like Si XI and Fe IX emitting at higher temperatures (see Sect. 2 for details). As a consequence both plasma cooling down after a flare or draining from a cool prominence can be visible in EIT 30.4 nm, as well as waves and instabilities propagating in plasma at these temperatures. Therefore, when no clear or evident cause is noticable nearby, the nature of intensity variations in this EUV band is not straightforward to understand.

Send offprint requests to: Anik De Groof,
e-mail: Anik.DeGroof@wis.kuleuven.be

Since the time cadence of the EIT instrument is limited in nominal mode, intensity variations with periods of the order of a minute can only be seen in the so-called 'EIT high-cadence synoptic program' or 'shutterless program'. This program, which was started in December 2000 by the Royal Observatory of Belgium (Clette 2000), takes every 3 months a high-cadence sequence of 120 images in shutterless mode[1], allowing for a time cadence of 68s. Instead of the normal full disk field of view, caught by a CCD camera of 1024×1024 pixels, the EIT shutterless program is limited to a subfield of 416×416 pixels (1 EIT pixel ≈ 2.6 arcsecs). The sequence is taken alternately in two bandpasses, 30.4 nm and 19.5 nm. The program is supported by TRACE (most often in 17.1 nm) and optionally by instruments as CDS, MDI or Coronas-F/SPIRIT. The technical details and the calibration needed for this EIT shutterless mode are described in Sect. 2 of De Groof et al. (2004) (hereafter referred to as Paper I).

In Paper I, we concentrated on the analysis of a specific EIT 30.4 nm shutterless campaign, carried out on 11 July 2001. The most intriguing feature present is an off-disk loop-like structure above active region NOAA 9538 which shows intensity variations propagating downward during the whole sequence. South of this loop, a smaller and more complex off-disk loop structure expands and brightens up while northwest of these two phenomena, a dark filament shows intensity variations moving northward along the spine of the filament connecting it to the part of the prominence seen off-disk. In addition, the east and north limb show several (macro) spicules and plasma flows along magnetic loops.

In our search for the origin and nature of the intensity variations, we compared the EIT 30.4 nm data with co-temporal data from TRACE (17.1 nm), Yohkoh-SXT (soft X-rays), the other EIT wavelengths (17.1 nm, 19.5 nm and 28.4 nm) and Big Bear Solar Observatory (Hα). As discussed in Paper I, GOES reported a C2.4 flare going off in the field of view under analysis with its peak occurring at 17:11 UT. This flare is seen in all the available data of EIT, Trace and SXT but it corresponds to the small loop structure expanding and brightening south of the downward motions we investigate here. Overplotting the EIT 30.4nm image with data available in higher temperatures than 304Å showed no sign of the loop-like structure under analysis nor the intensity variations. Also data from lower temperature plasma were investigated. Since the signal in the EIT 304Å bandpass is dominated by He II emission, we hoped to see similar plasma features in the Hα line which emits at chromospheric temperatures. Up to now, the EIT 30.4 nm data were only roughly compared to Hα data of Big Bear Solar Observatory. Nevertheless, similar intensity variations showed up in both wavelength bands so this could proof the EIT blobs to be cool plasma concentrations falling along magnetic field lines.

In the present paper, we continue the analysis of the downflows by a thorough investigation of the similarities between the bright blobs seen in EIT 30.4 nm and the ones in Hα. To the best of our knowledge, this is the first study in which movies of these two instruments are compared in a detailed manner. By carefully co-aligning EIT and Hα, we compare on a pixel-to-pixel basis the features observed by both instruments.

In the following section, the available data and the characteristics of both instruments/filters are described. The co-registration technique which is developed is described in Sect. 3 and applied in Sect. 4 for a detailed comparison of the EIT 30.4 nm and Hα downflows. In Sect. 5, the origin and the nature of the downflows is discussed and interpreted. All results are summarized in Sect 6.

2. Data description

The EIT 30.4 nm shutterless campaign, carried out on 11 July 2001, lasted from 16:00 UT until 18:28 UT and resulted in a sequence of 120 images, interrupted only by two gaps allowing each for a LASCO C2 image. The field of view of the 30.4 nm sequence under analysis is the northeast quarter disk, shifted one block (i.e. 32×32 pixels) to the east and one block to the south. The resulting FITS files consist of 416×416 pixels with a resolution of 2.6 arcsecs per pixel.

On the same day, the Big Bear Solar Observatory (BBSO), located in Big Bear Lake, California, took 1060 Hα images between 15:43 and 00:33UT at a cadence of 30 seconds (Denker et al. 1999). However, during the time EIT was observing as well (16:00-18:28UT), only the images taken between 17:45:15 and 18:11:15 and a few images around 16:30 are useful. The other images show a different FOV or contain too many technical defects and artifacts. Before these 56 full disk images could be compared with the EIT 30.4 nm data, the raw data were first calibrated by the BBSO team (Yurchyshyn - private communication), i.e. dark current subtraction, flat fielding and contrast enhancement were performed. The resulting FITS files of 2032×2032 pixels (1.05 arcsecs per pixel resolution) were then used as input for our analysis.

Since the emission recorded by EIT 30.4 nm and by BBSO is filtered in a different way, the comparison of the two wavelength bands reveals important information about the location and temperature of the plasma which is observed.

The 30.4 nm channel of EIT was designed to observe the transition region and the chromospheric network. Since it is a broad wavelength band (centred around 30.4 nm), plasma of different temperatures is observed. The dominating spectral line is the He II 30.4 nm line, which has an excitation temperature of about 6.0×10^4 K. However, especially in plasma at low densities, this line can emit as well at lower temperatures because of scattering of the disk radiation (e.g. Labrosse & Gouttebroze 2001). In addition, the EIT 30.4 nm bandpass also detects emission from Fe IX at 17.1 nm and from Si XI at 30.33 nm which results in a slightly weaker peak in the EIT response around one million K (see Fig. 9 in Delaboudinière et al. 1995). Whether emission caught on the CCD is due to hot or cool material can only be decided by comparing the EIT 30.4 nm images with

[1] The shutter is forced to stay open during the whole sequence of images so that a high cadence (68 s) and exposure time (≈ 50 s) can be established. On the other hand, this leads to unphysical smears throughout the image since the CCD pixels are read out while the shutter is still open so that photons falling in onto the CCD during the read-out process are still registered. Therefore an adapted calibration program is needed to clean the images (Berghmans 1998; De Groof et al. 2004).

images taken in other wavelength bands, e.g. by EIT 17.1 nm (the emission of which is dominated by the Fe IX line), and with the emission from cool chromospheric lines like the Ca II-line and Hα.

There is no such uncertainty for the light recorded on the Hα images. The 15 cm telescope at BBSO, monitoring the whole sun, is equipped with a very narrow bandwidth filter, centred on the Hα spectral line (656.28 nm). With a filter bandpass of 0.05 nm, only light close to the Hα wavelength is recorded.

In order to overlay the EIT and BBSO images and compare the features on a pixel-to-pixel basis, the two image series should be limited and rebinned in such a way that they show the same field of view with a comparable resolution, i.e. the same number of pixels. This co-registration technique must overcome the difference in wavelength, in spatial resolution (2.6 arcsecs per pixel for EIT vs. 1.05 arcsecs per pixel for BBSO), in time resolution (≈68s and 30s respectively), and in field of view (18.2×18.2 arcmins, roughly a quarter disk, and 35.7×35.7 arcmins, full disk, respectively). In addition, there are deformations of the images, indescribable in translations, which lead to a non-circular solar limb or a slight rotation of the solar disk around the solar centre. Especially the BBSO images, taken from Earth, suffer the most from these deviations.

3. Co-registration technique

3.1. Pixel to pixel transformation

The procedure we follow for the co-registration starts by selecting one BBSO image and one near-simultaneous EIT image. First, we 'zoom-in' on the part to be analysed: the selection of the interesting region is done in the BBSO image, in the EIT image a slightly larger region is selected so that all features visible in the BBSO selection are also included in the EIT selection.

Since, apart from the deformations described above, the differences between the two instruments and filters lead to differences in the plasma shown in the images, contrast, resolution, etc., standard techniques like cross-correlation are difficult to use. Therefore, we follow a totally different approach: with the aid of n pairs of corresponding points, i.e. n locations on the solar surface or in off-disk plasma which can be recognized in both wavelengths, we look for a transformation of the EIT pixels to the new BBSO field of view. The theory we apply to find the transformation between the n pairs of points is often cited as a *camera model for perspective images* (e.g. Semple & Kneebone 1979): points on the so-called 'world plane' are mapped to points on the 'image plane' (suffering from perspective projection) by a plane to plane homography, also known as a *plane projective transformation*.

Mathematically this theory is built up as follows. The homography is described by a matrix H. Once this matrix is determined, the back-projection of an image point to a point on the world plane is straightforward. Under perspective projection corresponding points are related by (Mundy & Zisserman 1992; Semple & Kneebone 1979):

$$\bar{X} = H\bar{x}, \tag{1}$$

where points on the world plane are represented by homogeneous coordinates $\bar{X} = (X, Y, Z)^T$, their corresponding images are represented by homogeneous coordinates $\bar{x} = (x, y, 1)^T$, and H is a 3×3 homogeneous matrix.

In our case we work with two images, one from Big Bear Solar Observatory, considered to be the 'world plane' and one from EIT, the 'image plane', which are two-dimensional and supposed to be parallel[2]. Therefore, we simplify the theory above by assuming all Z_i to equal 1 (the scale factor between both images can easily be derived at the end of the procedure). From there on we follow exactly the same procedure as used in the *camera model for perspective images*.

From Eq. 1, each pair correspondence provides two equations linear in the H matrix elements. We can use the fact that $\bar{X}$ and $H\bar{x}$ are parallel, or $\bar{X} \times H\bar{x} = 0$, to find

$$\begin{aligned} Yh^3\bar{x} - Zh^2\bar{x} &= 0, \\ Xh^3\bar{x} - Zh^1\bar{x} &= 0, \\ Yh^2\bar{x} - Zh^1\bar{x} &= 0, \end{aligned} \tag{2}$$

where $h^j (j = 1, 2, 3)$ is the j^{th} row of H and $Z = [1, 1, 1]^T$.

Only two of these three equations are linearly independent so we forget about the third and proceed with the first two. For n correspondences we obtain a system of $2n$ equations in 8 unknowns. If $n = 4$, an exact solution is obtained. Otherwise, if $n > 4$, the matrix is overdetermined, and H can be estimated by a suitable minimization scheme, like the least square algorithm. When the data are not perfect like in this case, it is better to use more than four points to calculate H.

The covariance of the estimated H matrix depends both on the errors in the position of the points used for its computation and the estimation method. In the most commonly used method, the non-homogeneous linear solution, one of the nine matrix elements is given the fixed value 1 and the resulting simultaneous equations for the other eight elements are solved using a pseudo-inverse. It has the disadvantage that poor estimates are obtained if the chosen element should have the value zero (Criminisi et al. 1999). Therefore, we use a different method to estimate H: the *singular value decomposition* (SVD). Writing the H matrix in vector form as $h = (h_{11}, h_{12}, h_{13}, h_{21}, h_{22}, h_{23}, h_{31}, h_{32}, h_{33})$, the homogeneous equations (2) for n points become $Ah = 0$, with A the $2n \times 9$ matrix:

$$A = \begin{bmatrix} x_1 & y_1 & 1 & 0 & 0 & 0 & -X_1x_1 & -X_1y_1 & -X_1 1 \\ 0 & 0 & 0 & x_1 & y_1 & 1 & -Y_1x_1 & -Y_1y_1 & -Y_1 1 \\ x_2 & y_2 & 1 & 0 & 0 & 0 & -X_2x_2 & -X_2y_2 & -X_2 1 \\ 0 & 0 & 0 & x_2 & y_2 & 1 & -Y_2x_2 & -Y_2y_2 & -Y_2 1 \\ \dots & & & & & & & & \\ x_n & y_n & 1 & 0 & 0 & 0 & -X_1x_1 & -X_1y_1 & -X_1 1 \\ 0 & 0 & 0 & x_n & y_n & 1 & -X_1x_1 & -X_1y_1 & -X_1 1 \end{bmatrix}$$

It is a standard result of linear algebra that the vector h that minimizes the algebraic residuals $\|Ah\|$, subject to $|h| = 1$, is

[2] Since SoHO follows an elliptic orbit around L1 and Big Bear Solar Observatory is located on Earth (California), the two image planes are not perfectly parallel. However, due to the large distance from the Sun, the maximum deviation angle between both planes is approximately $0,13^\circ$ or $0^\circ 07' 44"$ which justifies the assumption.

given by the eigenvector corresponding to the least eigenvalue of A^TA. This eigenvector can be obtained directly from the singular value decomposition of A: like every matrix, A can be written as a product of two orthogonal matrices $U \in \mathbb{R}^{2n\times 2n}$ and $V \in \mathbb{R}^{9\times 9}$ and a matrix $S \in \mathbb{R}^{2n\times 9}$:

$$A = USV^T,$$

where S consists of the diagonal matrix $diag(\sigma_1, \sigma_2, \ldots, \sigma_9)$, with σ_i an eigenvalue of A^TA, on the first 9 rows and zeros on the remaining $2n - 9$ rows (e.g. Bai et al. 2000; Golub & Loan 1996). The vector h can be found as the vector in V which corresponds to the location of the smallest eigenvalue in S. This vector totally determines the transformation matrix H between the 'world plane' and the 'image plane'. A scale factor found from the ratio between the coordinates of the original points and the transformed points then completes the transformation.

3.2. Application to the EIT and BBSO image series

We now apply the theory described above to the two image series we want to compare. As explained before, we start with one BBSO image and one EIT image which are near-simultaneous. We consider a selected part of the BBSO Hα image as the 'world plane' and a similar (but larger) selection of the EIT 30.4 nm image as the 'image plane'. We choose five locations in the solar plasma which can be recognized in both wavelengths and determine the five corresponding pairs of coordinate vectors, $(X_i, Y_i)^T$ in Hα and $(x_i, y_i)^T$ in EIT ($i = 0, \ldots, 4$). The images we choose to calculate the transformation matrix are the Hα image taken at 17:53:45UT and the EIT 30.4 nm image of 17:53:57UT. In Fig. 1, the selected area of the Hα image is shown on the left and a similar but slightly larger selection of the EIT image is shown on the right. Both images are enhanced or calibrated in a special way to show maximal contrast. More details about these techniques are given in Sects. 4.1 and 4.2. To simplify the rest of the algorithm, we rescale both images to 400×600 pixels.

In the next step we choose five corresponding points in each image and mark them by crosses. It is important to choose these points as far apart as possible in order to increase the quality of the transformation. In addition solar features must be carefully compared since both images are taken in different wavelengths so that e.g. loops observed in one image do not always correspond to the loops visible in the other image.

The coordinates of the five points in the EIT image are now transformed to the BBSO image by calculating the transformation matrix H (see algorithm above). The ratio between the coordinates of the five BBSO points and the coordinates of the transformed EIT points determines the scale factor. In order to validate the transformation, we plot in Fig. 2 (left) the marked points of BBSO together with the transformed EIT points on the BBSO Hα image. The small differences in the location of the crosses are mainly due to the errors made in the positioning of corresponding data points.

The last step now consists of transforming the whole EIT image (or better, the part which really corresponds with the BBSO selection) to the coordinate system used for the BBSO image. Since the EIT selection to be transformed has slightly less than 400×600 pixels, transforming it to a new 400×600 pixel field leads to oversampling. This problem is solved by first rebinning the EIT image to the double size (filling the even rows and columns by an interpolation program). The result is shown in Fig. 2: the transformed EIT 30.4 nm image is shown on the right hand side and can be compared with the Hα image on the left.

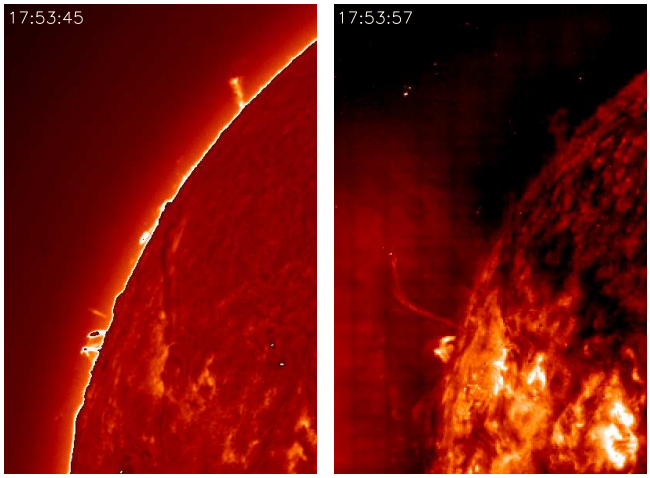

Fig. 1. Left: The processed Hα image taken at 17:53:45 UT. The brightness of the off-disk region is enhanced in order to clearly show both the features on- and off-disk (see Sect. 4.1). Right: The partially calibrated EIT 30.4 nm image at 17:53:57 UT (see Sect. 4.2). Only the subfield which is selected to be transformed is shown.

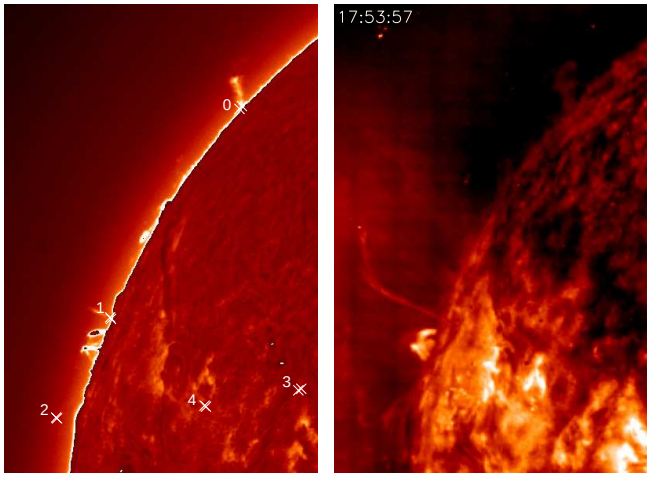

Fig. 2. Left: The BBSO selection showing the marked points in this image, together with their counterparts which are marked in EIT and transformed to the BBSO coordinate system. Right: The EIT 30.4 nm selection after transformation, showing the same field of view as the BBSO image on the left.

4. Detailed comparison of both data sets

As described in the introduction, the solar activity we want to analyse and compare in different wavelengths shows up as intensity variations propagating downward for at least two hours along an off-disk loop structure (see Paper I for more details). This feature, interpreted as downflows in Paper I, resembles a train of bright blobs moving down the magnetic loop struc-

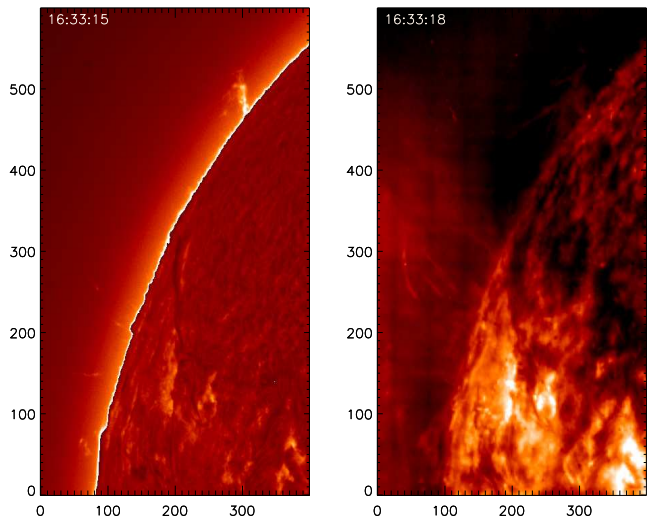

Fig. 3. Left: Hα image of the north-eastern quarter disk at 16:33:15 UT. The brightness of the off-disk region is enhanced in order to clearly show both the features on- and off-disk. Right: Calibrated EIT 30.4 nm image of the off-disk-loop region at 16:33:18 UT.

ture, both in the EIT 30.4 nm shutterless sequence (where seven blobs were defined) as in the Hα data.

Since we deal with moving features, the co-registration of these data sets should be seen over a wider time span. Therefore the only way to visualize the similarities and differences in both wavelengths is to overlay both image series in such a manner that the bandpass in which each feature was observed is still visible and, on the other hand, overlapping features (present in both data sets) are clearly recognized. We tested different kinds of visualization techniques and evaluated these in terms of contrast, visibility of overlapping features, stability (in movies), etc. Before we start overplotting both image series, we try to find the best possible presentation of both images separately.

4.1. Visualization of BBSO Hα images

Although we are especially interested in the off-disk region, the standard processing of BBSO Hα data aims to maximally enhance the on-disk features. Therefore we have to enhance the off-disk region intensity while the on-disk region is left unchanged. We define the limb in the images as the collection of pixels where the intensity equals a certain limiting value. All pixels with intensities above this value are defined as lying on-disk, while all pixels which are darker belong to the off-disk region. The intensity of the latter can then be enhanced in order to show all interesting features both on and off-disk. The result is shown in Fig. 3 (left), where only the region selected in Sect. 3 is depicted. The same technique is used to visualize the Hα image in Figs. 1 and 2 (left), taken at a later time. Note that due to the fixed intensity value set as limiting boundary between the on-disk and off-disk region, some very bright off-disk regions like the flare loops show (unphysical) intensity jumps.

4.2. Visualization of EIT 30.4 nm images

Raw EIT shutterless images show a lot of noise and artifacts due to the telescope's aging and the peculiar use of the instrument during a shutterless program. The unphysical smears caused by the open shutter and the corresponding calibration techniques are described in detail in Paper I. Apart from the smear, the sequence should also be corrected for the standard contaminations due to the instrument itself. Since the standard 'EIT_PREP'-program (available in the IDL Solar Soft Library) cannot be applied on shutterless sequences, we use similar IDL techniques, implemented directly into the code we designed to read, calibrate and analyse the series of images. The best results are found after correcting for missing blocks, flat field emission, traces of the grid, and after the application of a filter factor correction. Since the *normal response function* applied in EIT_PREP is not adapted to the extra complications of shutterless images, we choose to skip this correction in order to keep an optimal contrast in the images and more specifically in the downflow region. The resulting EIT 30.4 nm image of the selected and co-registered region is shown in Fig. 3 (right). As a consequence of the incomplete correction, part of the grid structure is still visible off-disk. Again the same technique is used in Figs. 1 and 2 (right).

By comparing the two near-simultaneous images in Fig. 3, several similarities can be found. In the next subsection we will study them in detail by overlaying both images by means of different visualization techniques.

4.3. Overplotting both image series

A first technique we use to visualize the correspondence between the images is to overplot the BBSO data with a contour plot of EIT. In Fig. 4 (left) two images taken by both telescopes around 17:55 UT are corrected in the way described above and overplotted by means of a contour plot. The corresponding features seen by both instruments, like the downflow region, the flare loops and the prominence off-disk, together with some bright regions on-disk, seem to match very well. Nevertheless, contours tend not to show all the information available because contour lines are too far apart, while on the other hand additional contour lines make the plots too messy and are too overwhelming when used in movies (see on-line movie 'eitoverbb-contour.gif'). This visualization technique is perfect to study the data of one instrument in detail with the data of the other instrument (in contour lines) as background or as reference. However, when the full information available in the two datasets is important, this technique does not satisfy all needs.

A second technique which can be used to overlay two similar images consists in displaying each image in one particular colour channel, for example one image in red and the other in green. In this way, features which are only visible in one of the two images show up in the original colour of that image, red or green, while overlapping features get a composite colour, yellow in this case. For this technique, it is important that both images are displayed with a similar brightness to avoid that overlapping features are not recognized due to a

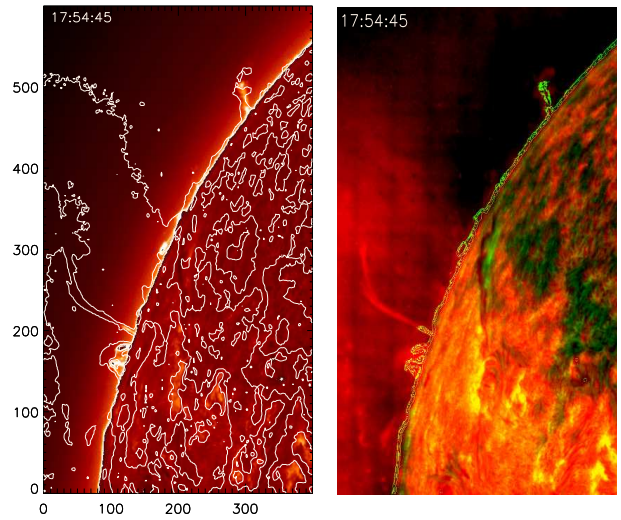

Fig. 4. Left: Hα image of the off-disk-loop region at 17:54:45, overplotted by the contours of EIT 30.4 nm at 17:55:05. The contour north of the flaring loop corresponds with the downward motion in EIT. Right: Idem but overplotted in colour coding.

dominant brightness in one of the two channels. However, the width and peaking of the wavelength band filtered by each instrument can cause certain plasma temperatures or densities to show up very brightly in the one and quite weak in the other image. On one hand, this is an excellent tool to extract information about the characteristics of the plasma we are observing. On the other hand, this complicates the technique of overplotting since some features visible in one channel could be hidden by their dominant brightness in the other channel. Therefore the individual images should never be exluded from the analysis.

Taking this into account, the results are very promising. In Fig. 4 (right), we overplot the same images as used in Fig. 4 (left) but now in colour coding. Only for the visualization of the Hα image, an extra tool is used. Apart from the enhanced off-disk region, the intensities in this region are shown with the aid of the edge-detection procedure Sobel. This means that, instead of showing the pixel intensities themselves, the largest gradients in intensity are detected and marked by bright lines. In this way the fairly weak falling blobs, moving along the PD-loop (see Sect. 1) are better visible. This technique gives very good results when used in movies (see on-line movies 'eitoverbb-col1.gif' (with edge-detection) and 'eitoverbb-col2z.gif' (zoomed, without edge-detection)).

4.4. Comparison of downflows: blobs and speeds

As shown by the movies, the sequence of downflowing blobs that was first seen in the EIT 30.4 nm (Paper I) is perfectly recognizable in the co-registered Hα images. This proves that the phenomenon is indeed of chromospheric nature and not a coronal contribution of the Si XI line in the EIT bandpass. An extra argument to draw this conclusion is found by comparing the speeds of the blobs seen in EIT 30.4 nm and Hα. The speeds of the EIT blobs were analysed in Paper I and found to form a compact cloud of speeds increasing from roughly 40 km s^{-1} at the top of the loop (100 Mm) to about 120 km s^{-1} near the limb (see Fig. 7 in Paper I). These measurements were done by fitting the slope of the bright ridges showing up in a location-time plot (Fig. 6 of Paper I). In Fig. 5, a similar location-time plot is made, now for Hα . First we outline the track that most of the blobs are following (see Fig. 5-left) and collect the intensity information of each pixel along the track and the pixels in its direct neighbourhood for each frame in the sequence. All counts in a box of 5 by 5 pixels around each track pixel (spanning 5 arcsec) are summed together and used to construct the intensity profile along the track at time t. The set of these profiles for each moment in time are combined as columns in the location-time plot in Fig. 5 (right). Time is plotted on the horizontal axis. Since the overall brightness of the plot was chosen in order to show as many features as possible, the brightest region of the plot is saturated. Therefore we also include a close-up of this region as an inset in Fig. 5 (right).

When compared to Fig. 6b of Paper I, this plot is limited in time. The Big Bear Hα images are only available from 17:45 to 18:11 which leads to a restriction to the so-called blobs 5 and 6 seen in the EIT data. The downward movement of these two blobs along the loop track shows up in Fig. 5 (right) as the two bright ridges with a negative slope, running from the upper left corner of the image to the bottom (see labels B5 and B6 in the figure). There is also a limitation in space because the blobs are not seen as far from the limb as in the EIT 30.4nm images. Therefore a comparison can only be made with the speeds found for the EIT blobs 5 and 6, and up to a height around 60000 km above the limb.

By measuring the slopes of each ridge at several locations along the loop (marked by the numbers in the left figure and the horizontal solid lines in the right figure), we can calculate the apparent[3] speed (plane-of-sky speed) of the intensity variations at each location. In order to compare the speeds of the Hα blobs shown here with the speeds measured in the EIT images, we overplot the bright ridges in Fig. 5 (right) with straight blue lines which slopes correspond to the EIT blob speeds. Each line is centred on the location where the speed was measured (these locations are indicated by horizontal dashed lines in the figure). As it is clear from this figure, these lines outline the Hα bright ridges almost perfectly which means that the speeds measured in Hα and EIT 30.4 nm match very well.

We also put the newly measured speed values on a location-speed plot (similar to Fig. 7 in Paper I). Fig. 6 shows the measured speeds of each 'blob', in EIT 30.4 nm and Hα, at several locations along the loop. The locations at which speeds were measured in the Big Bear Hα data (for blobs 5 and 6) are indicated by arrows at the bottom of the figure. Again there is a good agreement between the speeds measured in both wavelengths. The uncertainties close to the limb are due to the often broad base of the bright ridges in the location-time diagrams.

[3] We write 'apparent' since, taking into account the line-of-sight projection effects, the measured values are only a lower limit for the true propagation speeds.

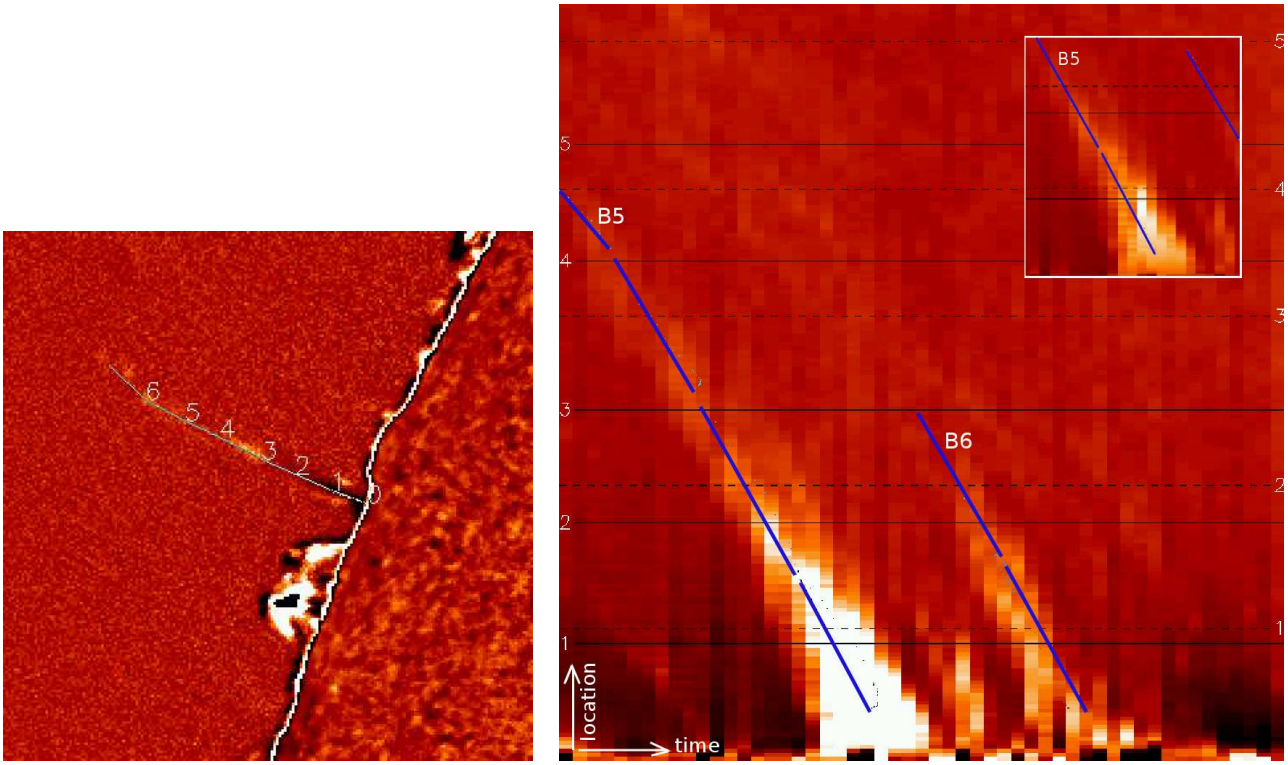

Fig. 5. Left: The track of the intensity variations, outlined in one frame of the Hα -sequence (at 17:49). Right: Location-time plot of the outlined track. The location numbers in the left figure correspond to the numbered horizontal solid lines on the right. The horizontal dashed lines correspond to the locations where velocities were measured in the EIT images. The slopes of the blue lines correspond with these velocities. The inset shows a less bright close-up of the base of blob 5.

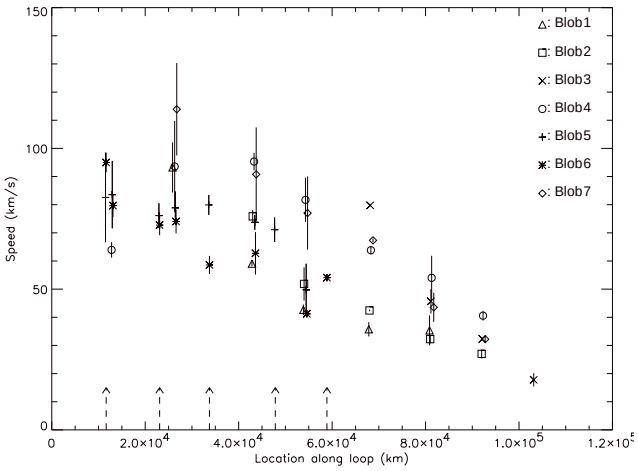

Fig. 6. The measured speeds of each 'blob' at several locations along the loop. The arrows point to measurements done in Hα .

The co-registered movies and Figs. 5 and 6 show that the blobs seen in the two wavelengths fall at the same time and with the same speed downward along the loop-like structure, which leads to the conclusion that the same plasma blobs (or at least parts of the same plasma concentrations, at slightly different temperatures) are seen in both wavelengths.

4.5. Comparison of downflows: blob appearance

Although the speeds of the blobs seen in both wavelenghts match very well, the way the blobs show up in both image series is clearly different, as illustrated by Fig. 7. In four subsequent images the touchdown of the fi fth blob in the EIT shutterless sequence (see Paper I) is shown, as observed by Big Bear Solar Observatory in Hα (top row), and by EIT 30.4 nm (middle). The bottom row of images shows both images at the same time, overplotted using the colour coding technique (without edge-detection). Although we know from Fig. 6b in Paper I and from the movies that the blobs are clearly separated, in the EIT 30.4 nm images of Fig. 7 blob 5 seems to almost have merged with the following blob coming down. For this reason white circles are drawn in the EIT 30.4 nm images pointing to the parts related to blob 5 which thus can be compared with the bright part of the loop in the Hα images. Blob 6 does show up in the Hα images as well, viz. in the image taken at 17:58:15UT, as the weak brightening just above the bright end of blob 5 touching down at the solar surface (see also Fig. 5).

It is clear from Fig. 7 that a few pronounced differences are seen in the appearance of the blobs in the two datasets. In general, the Hα blobs are smaller and more compact than the bright plasma in EIT 30.4 nm. Secondly, EIT 30.4 nm shows much more material higher up as compared to Hα. The BBSO Hα images only show blobs close to the limb, even while some blobs higher up are very bright in EIT 30.4 nm. Apart from these general differences, Fig. 7 also illustrates a different behaviour in time: only in Hα, the blob brightens up while falling

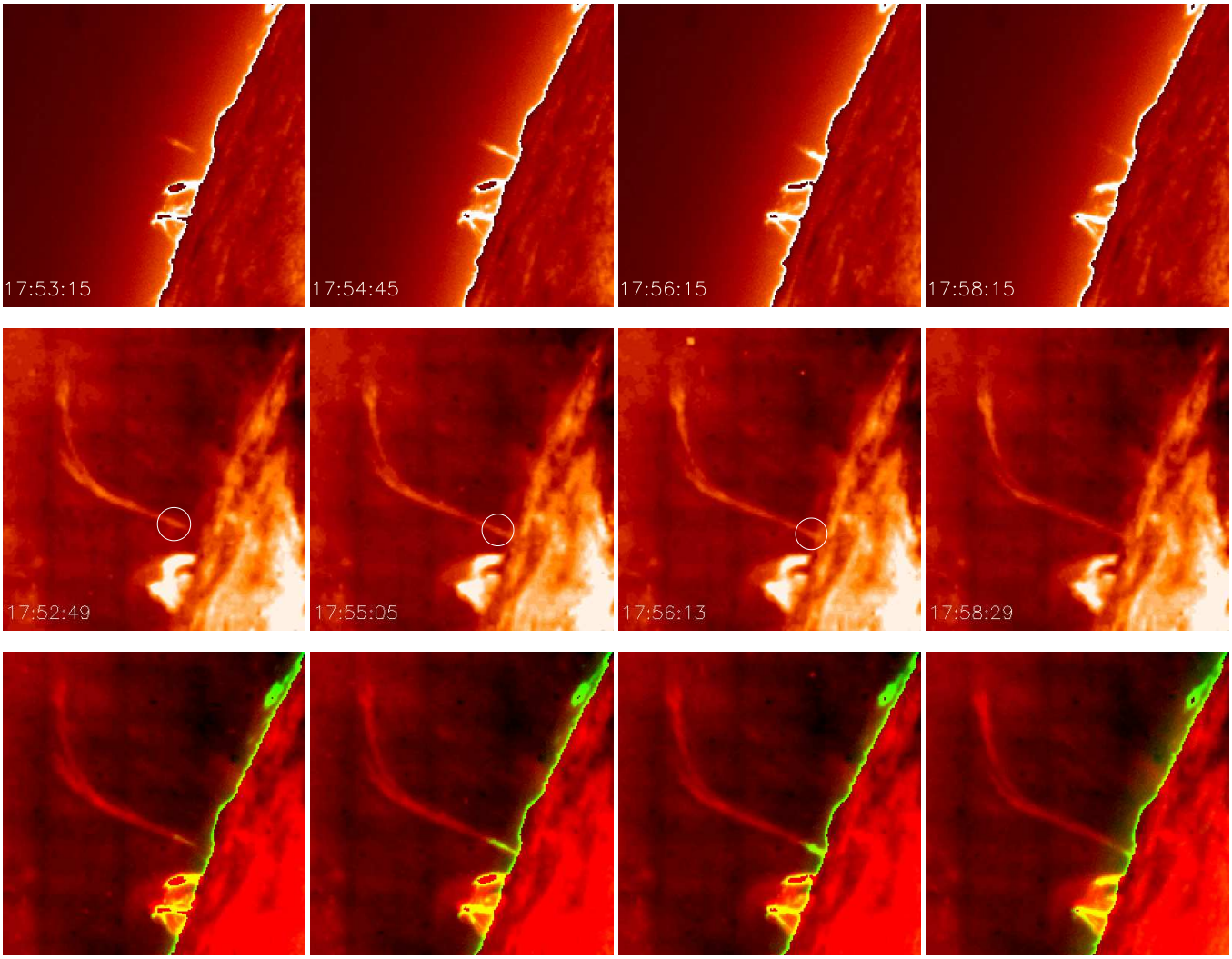

Fig. 7. Touchdown of blob 5 in the BBSO Hα images (top) and in the EIT 30.4 nm images (middle). The white circle in each eit304 image points to the part which is related to this particular blob. The bottom row shows the overplotted images in colour coding.

down. In EIT 30.4 nm, the blob's intensity does not change signifi cantly and most blobs even disappear in 30.4 nm before they touch the solar surface.

Since these differences might reveal a lot about the plasma being observed, sound arguments should be found in order to explain the nature of the downfbws. The reason why the blobs in Hα are smaller and more compact than in EIT 30.4 nm might be that EIT 30.4 nm shows plasma in a much wider temperature band than Hα. Only the coolest parts of the EIT blobs show up in Hα and due to the increasing radiative loss in denser plasma, these parts are likely to be the 'cores' of the blobs (see also Sect. 5).

The difference in intensity high above the limb, on the other hand, could have several reasons. First it could be an instrumental effect since Big Bear Solar Observatory is not designed to see any features off-disk. By the contrast enhancement techniques described in Sect. 4.1, we were able to detect some features close to the limb but any features further out could still be hidden. This could also explain why the blobs look brighter closer to the limb.

Another reason might be that the blobs high up are still too hot to show up in Hα while they have cooled down at the time they nearly reach the limb. This explanation is also supported by the fact that for several blobs, at touchdown, the footpoint shows up bright only in Hα and not in EIT 30.4 nm.

Finally, it is possible that cool blobs higher up in the loop are not seen in Hα because the loop structure is bended at larger heights so that the line-of-sight velocity of the blobs causes a shift of the Hα emission off-band of the narrow fi lter. This happens frequently in prominence observations.

The third important difference, the variation in the blobs' intensity while falling down, could be caused by an instrumental effect, as explained before, or by the effect of a cooling loop (see Sect. 5 for details and cooling times). However, especially close to the limb, the varying intensity of the blobs could also be caused by the so-called 'Doppler-brightening' (in case of Hα) and 'Doppler dimming' (He II 30.4 nm). These brightness changes are induced by velocity-dependent variations in the atomic-level populations and consequently in the radiation intensity in the wavelenghth range of the instrument's fi lter.

Heinzel & Rompolt (1987) showed that these effects can play an important role provided that the vertical velocity is of the order of 100 km s^{-1} or more and the density is not too high so that the scattering of the disk radiation dominates the line source function.

Apart from the differences there is also a remarkable similarity between the downflows in the two wavelength bands. Both image series do not show any brightening or change in the plasma on-disk at the time a blob comes down. Probably the blobs fall down just behind the limb and as a consequence the real footpoint is invisible for the two instruments.

5. Interpretation of origin and nature of the falling blobs

As discussed before, the bright blobs seen in EIT 30.4 nm and Hα are most likely due to cool plasma concentrations falling along magnetic field lines. A promising theory which could explain the origin of these mass blobs is the so-called 'heating-condensation-evaporation cycle', first described by Antiochos et al. (2000) for a prominence configuration and later extended to coronal loops by Müller et al. (2003). It is based on the fact that a magnetic loop which is predominantly heated at the footpoints becomes thermally unstable and rapidly cools down at the apex. Due to the associated pressure drop high up in the loop, plasma is evaporated into the coronal loop which then cools rapidly due to a loss of thermal equilibrium. The confined region of "condensed" plasma subsequently falls down under the effect of gravity in the form of a cool plasma blob. When the mass blob encounters the transition region, it compresses the underlying plasma and is thereby decelerated. Finally, the depleted loop reheats and fills up again by chromospheric evaporation and a new cycle starts.

This idea could easily explain the falling bright blobs seen in 30.4 nm. The numerical simulations of Müller et al. (2003, 2004), carried out with a 1D implicit hydrodynamic code with adaptive grid, indeed show plasma condensations and high-speed downflows in (cool) coronal loops, using a very simple, *time-independent* heating function. Depending on the spatial distribution of the energy deposition in the loop, the evolution is static, periodic or irregular. Since the non-equilibrium rate equations for any desired atomic species are solved simultaneously with the hydrodynamic equations, the time-dependent emission of optically thin UV emission lines can be synthesized and compared to the observations. These simulations, first performed in a loop of 100 Mm, show a lot of similarities with the observations (see Fig. 13 in Müller et al. 2004). After the time the loop needs to become unstable has elapsed, a condensation region appears at the loop apex. It grows and falls down under gravity along both loop legs (or along one leg, depending on the symmetry of the loop, possible sound waves propagating through, etc.). When the condensation region encounters the transition region, it slows down or even bounces back, before it reaches the solar surface ($z = 0$). Compared to our observations, the results of Müller et al. (2003, 2004) were very encouraging in the sense that the formation of such high-density regions was indeed possible without any time-dependent driving mechanism. On the other hand, the simulations mostly showed only one falling blob with a velocity of 30-40 km s^{-1} which is lower than the observed ones (up to 120 km s^{-1}, see Fig. 6).

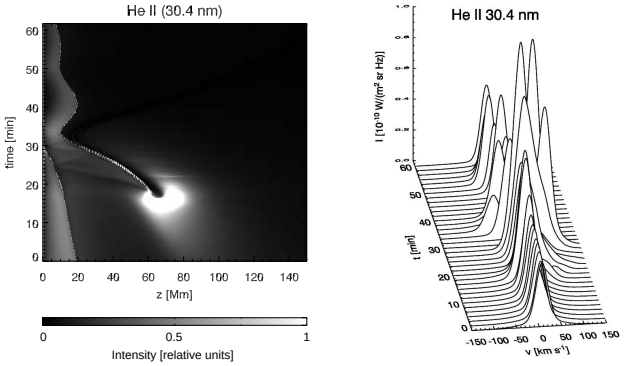

Fig. 8. Left: He II emission in a loop of 300 Mm (apex at z=150 Mm, only the left half of the loop is shown). Right: Line profiles of He II in a 300 Mm loop during the fall of the condensation region (Müller et al. 2005).

In a subsequent paper (Müller et al. 2005), the simulations were performed in a loop geometry inferred from the EIT 30.4 nm data ($L \approx 300$ Mm). In addition a higher heating rate was used to reach more realistic apex temperatures for large active region loops. Applying the catastrophic cooling scenario to these more appropriate models reveals that the rebound shocks caused by rapid cooling processes in hot loops can trigger further cooling events. The associated condensation regions, showing up as subsequent cool plasma blobs, are initially travelling with almost free-fall speed and can reach velocities of the order of 100 km s^{-1} before their deceleration sets in in the lower regions of the atmosphere. This is shown in Fig. 8 where the emission in the He II line[4] is plotted in order to compare with the observations in the EIT 30.4 nm data. In the left plot, which shows the emission integrated over the spectral line profile, two blobs are visible which follow close to one another. The first blob was formed outside this plot and moved slowly downwards (it first appears in the plot around a height of 20 Mm). When encountering the transition region, the subsequent rebound shock triggers another catastrophic cooling process which forms a second blob, visible in He II at an arclength around 70 Mm. This second blob moves much faster and bounces back when encountering the denser parts of the atmosphere. In the right plot, the varying velocity of the condensation region can be deducted from the line profiles of He II. For this plot, the emission is spatially integrated over the loop-half where the blob is falling down, assuming a view straight from above.

The simulations indeed give a theoretical explanation for the intensity variations seen in the EIT 30.4 nm and Hα observations. The cool blobs are manifestations of a rapid cool-

[4] The emission for this plot is calculated in an effectively thin plasma where the radiative losses are assumed to be entirely due to collisional excitation followed by spontaneous radiative decay. No scattering is taken into account which may affect the emission in the He II 30.4 nm line.

ing process which sets in without any time-dependent driving mechanism. The fact that the blobs are first seen in EIT 30.4 nm, forming close to the apex, and only later in Hα (which has a lower formation temperature) is a consequence of this cooling process. This idea also explains why the Hα blobs are seen to brighten up while falling down. Quantitatively, the radiative cooling time-scale for a 300 Mm hot loop, cooling down from 2.5MK purely due to radiative losses, is calculated to be about 180 minutes (see Eq. 3 in Schrijver 2001). For comparison, the downflow time-scale for the fast blob in the 300 Mm model from the first appearance in Fig. 8 (left) around 62 Mm to a height around 10 Mm where the blob is strongly decelerated, is 17 minutes. This proves that the moving blobs are not simply cooling fronts moving downwards. (If one considers the time-scale starting from the blob's formation - the first subtle local maximum in the radiative losses - until the blob finally drains around 7 Mm height, one gets about 60 min (see Fig. 5 and 6 in Müller et al. 2005).)

Finally, the train of subsequent bright blobs can be explained by rapid cooling processes in parallel loop structures or by rebound shocks triggering subsequent and often much faster blobs. The location-time plot of the EIT 30.4 nm data indeed indicates significant differences in the speeds of subsequent blobs. There even seem to be events where fast blobs catch up with slower ones (see Fig. 6 in Paper I), but further analysis of more data sets is needed to confirm or reject this hypothesis.

6. Summary

In this paper we studied in detail two high-cadence, co-temporal data sets of off-disk intensity variations along a half loop, taken at 11 July 2001. The first image series was taken by EIT (in shutterless mode) in a broad wavelength band around 30.4 nm, the second was taken from earth by Big Bear Solar Observatory at the wavelength of Hα, λ=656.3 nm. Both data sets show bright blobs moving down at similar (increasing) speeds. In order to compare them in more detail, we first designed a co-registration technique which coaligns both image series as good as possible in space and time (Sect. 3). As a next step, in Sect. 4, several visualization techniques were tested in order to show both types of images with maximal contrast and similar brightness. In this way, both image series could be overplotted in order to study similarities and differences in space and time. In this particular example the second technique using colour coding was found to give the most satisfying result.

These co-registration and visualization techniques were then used to compare the behaviour of the plasma blobs in the EIT 30.4 nm and the BBSO Hα images (Sect. 4.5). We concluded that the same cool plasma is seen by both instruments but due to differences in the width of the spectral window and consequently in the temperature of the plasma observed, the blobs show up in a different way in both image series.

All results support the idea of the bright blobs being cool plasma condensations falling under gravity. The most promising theory to explain the origin of the blobs is the 'heating-condensation-evaporation cycle' simulated in long coronal loops by Müller et al. (2005). Simulations done in loops comparable to the PD-loop show condensation regions and high-speed downflows comparable to the ones observed in EIT 30.4 nm and BBSO Hα. However, more high-cadence observations of off-disk coronal loops are needed to confirm or reject the catastrophic cooling scenario. The distribution of blob speeds as a function of height above the limb should be studied and compared to the theory. For example observations of blob speeds which are first increasing and then decreasing close to the solar limb, would strengthen the concept of falling plasma condensations. However, observations of blobs approaching the limb at high speeds (close to free-fall) don't necessarily reject this hypothesis; this could indicate that part of the loop underneath the falling blob has been evacuated by a different process.

Since the basis of the catastrophic cooling theory is a continuous (time-independent) heating at the coronal footpoints, an extended investigation could give us important insight in the nature of the heating mechanism(s) acting in the overall corona.

Acknowledgements. We would like to thank Vasyl Yurchyshyn for the provision and calibration of the BBSO Hα images. The authors are very grateful to Bogdan Nicula for the idea of the plane projective transformation and to the referee who provided a lot of extra information and suggestions which led to a real improvement of the paper.

References

Antiochos, S. K., MacNeice, P. J., & Spicer, D. S. 2000, ApJ, 536, 494

Aschwanden, M. J., Fletcher, L., Schrijver, C. J., & Alexander, D. 1999, ApJ, 520, 880

Bai, Z., Demmel, J., Dongarra, J., Ruhe, A., & van der Vorst, H., eds. 2000, Templates for the Solution of Algebraic Eigenvalue Problems: a Practical Guide (Siam, Philadelphia)

Berghmans, D. 1998, Data Preprocessing. Understanding the contaminations in the shutterless mode of EIT, Tech. rep., Royal Observatory Belgium, sol.oma.be/High-cadence/data-preprocessing/index.html

Clette, F. 2000, High-cadence synoptic program of the Extreme-ultraviolet Imaging Telescope, Tech. rep., Royal Observatory Belgium, sol.oma.be/High-cadence/

Criminisi, A., Reid, I., & Zisserman, A. 1999, Image and Vision Computing (IVC), 17, 625

De Groof, A., Berghmans, D., Van Driel-Gesztelyi, L., & Poedts, S. 2004, A&A, 415, 1141

De Moortel, I., Hood, A., Ireland, J., & Walsh, R. 2002a, Solar Phys., 209, 89

De Moortel, I., Ireland, J., Walsh, R., & Hood, A. 2002b, Solar Phys., 209, 61

Delaboudinière, J.-P., Artzner, G. E., Brunaud, J., et al. 1995, Solar Phys., 162, 291

Delone, A., Makarova, E., Porfiréva, G., Roschina, E., & Yukinina, G. 1989, Hvar Observatory Bulletin, 13, 157

Denker, C., Johannesson, A., Marquette, W., et al. 1999, Solar Phys., 184, 87

Engvold, O., Jensen, E., & Andersen, B. N. 1979, Solar Phys., 62, 331

Golub, G. H. & Loan, C. F. V., eds. 1996, Matrix Computations (The Johns Hopkins University Press, Baltimore and London)

Heinzel, P. & Rompolt, B. 1987, Sol. Phys., 110, 171
Heinzel, P., Schmieder, B., & Mein, P. 1992, Solar Phys., 139, 81
Labrosse, N. & Gouttebroze, P. 2001, A&A, 380, 323
Loughhead, R. E. & Bray, R. J. 1984, ApJ, 283, 392
Müller, D. A. N., De Groof, A., Hansteen, V. H., & Peter, H. 2005, A&A, 436, 1067
Müller, D. A. N., Hansteen, V. H., & Peter, H. 2003, A&A, 411, 605
Müller, D. A. N., Peter, H., & Hansteen, V. H. 2004, A&A, 424, 289
Mundy, J. & Zisserman, A. 1992, Geometric Invariance in Computer Vision (MIT Press)
Roberts, B. R. 2000, Solar Phys., 193, 139
Schrijver, C. J. 2001, Sol. Phys., 198, 325
Semple, J. & Kneebone, G. 1979, Algebraic Projective Geometry (Oxford University Press)
Wiik, J. E., Schmieder, B., Heinzel, P., & Roudier, T. 1996, Solar Phys., 166, 89